



HAL
open science

Synthesis of 2D perovskite crystals via progressive transformation of quantum well thickness

Jin Hou, Wenbin Li, Hao Zhang, Siraj Sidhik, Jared Fletcher, Isaac Metcalf, Surendra B. Anantharaman, Xinting Shuai, Anamika Mishra, Jean-Christophe Blancon, et al.

► To cite this version:

Jin Hou, Wenbin Li, Hao Zhang, Siraj Sidhik, Jared Fletcher, et al.. Synthesis of 2D perovskite crystals via progressive transformation of quantum well thickness. *Nature Synthesis*, 2023, 3 (2), pp.265-275. 10.1038/s44160-023-00422-3 . hal-04262698

HAL Id: hal-04262698

<https://hal.science/hal-04262698>

Submitted on 31 Oct 2023

HAL is a multi-disciplinary open access archive for the deposit and dissemination of scientific research documents, whether they are published or not. The documents may come from teaching and research institutions in France or abroad, or from public or private research centers.

L'archive ouverte pluridisciplinaire **HAL**, est destinée au dépôt et à la diffusion de documents scientifiques de niveau recherche, publiés ou non, émanant des établissements d'enseignement et de recherche français ou étrangers, des laboratoires publics ou privés.

1 **Deterministic synthesis of phase-pure 2D perovskite crystals via** 2 **progressive transformation of quantum well thickness**

3 Jin Hou¹, Wenbin Li^{2,3}, Hao Zhang^{2,3}, Siraj Sidhik¹, Isaac Metcalf¹, Surendra B.
4 Anantharaman⁴, Xinting Shuai,¹ Anamika Mishra,² Jean-Christophe Blancon², Claudine
5 Katan⁵, Deep Jariwala⁴, Jacky Even⁶, Mercuri G. Kanatzidis⁷ and Aditya D. Mohite^{1,2*}

6 ¹Department of Materials Science and NanoEngineering, Rice University, Houston, Texas
7 77005, USA.

8 ²Department of Chemical and Biomolecular Engineering, Rice University, Houston, Texas
9 77005, USA.

10 ³Applied Physics Graduate Program, Smalley-Curl Institute, Rice University, Houston, TX,
11 77005, USA.

12 ⁴Department of Electrical and Systems Engineering, University of Pennsylvania,
13 Philadelphia, PA 19104, USA.

14 ⁵Univ Rennes, ENSCR, INSA Rennes, CNRS, ISCR (Institut des Sciences Chimiques de
15 Rennes) - UMR 6226, F-35000 Rennes, France.

16 ⁶Univ Rennes, INSA Rennes, CNRS, Institut FOTON - UMR 6082, 35708 Rennes, France.

17 ⁷Department of Chemistry and Department of Materials Science and Engineering,
18 Northwestern University, Evanston, Illinois 60208, USA.

19
20 **Two-dimensional (2D) multilayered halide perovskites have emerged as a platform for**
21 **understanding organic-inorganic interactions, tuning quantum confinement effects and**
22 **realizing efficient and durable optoelectronic devices. However, a major bottleneck has been**
23 **reproducibly producing 2D perovskite crystals with desired perovskite-layer thicknesses**
24 **(quantum well thickness, also known as n values) greater than two with the existing crystal**
25 **growth methods. Here, we demonstrate a novel method termed kinetically controlled space**
26 **confinement (KCSC) for the deterministic growth of phase pure Ruddlesden-Popper (RP)**
27 **and Dion-Jacobson (DJ) 2D perovskites. The phase-pure growth is achieved by progressively**
28 **increasing the temperature (for a fixed time) or the crystallization time (fixed temperature),**
29 **which allows for acute control of the crystallization kinetics. In-situ photoluminescence**
30 **spectroscopy and imaging suggest that the controlled increase in n-value (from lower to**
31 **higher values of n=4, 5, and 6) occurs due to intercalation of excess precursor ions. Based on**
32 **data from 250 experimental runs, phase diagrams for both RP and DJ perovskites have been**
33 **constructed to predict the growth of 2D phases with specific n-values, facilitating the**
34 **production of 2D perovskite crystals with desired layer thickness.**

35

36 Two-dimensional halide perovskites (2D-HaP) have emerged as a new class of highly durable
37 solution-processed organic-inorganic (hybrid) low-dimensional semiconductors.¹⁻³ They exhibit a
38 unique combination of properties derived from four exciting classes of materials - quantum wells,⁴
39 atomically thin 2D materials⁵, organic semiconductors^{6,7}, and 3D-HaP perovskites^{8,9}. The general
40 chemical formula of 2D-HaP is $(A')_m(A)_{n-1}M_nX_{3n+1}$ (where A' is a bulky organic cation, A is a
41 small organic cation, M is a divalent metal, X is a halide, with $m=2$ in Ruddlesden-Popper (RP)
42 phases and $m=1$ in Dion-Jacobson (DJ) phases, and n determines the thickness of the perovskite
43 layer), which consists of alternate layers of organics $(A')_m$ and hybrid $(A)_{n-1}M_nX_{3n+1}$, providing a
44 perfect platform to engineer hybrid composites with attractive optoelectronic properties. There is
45 growing consensus that their physical properties are dictated by the interaction between the organic
46 cation and the inorganic framework, which presents a unique opportunity to understand and tailor
47 their behaviors,¹⁰ including, charge-carrier mobility,^{11,12} nonlinear optical effects,¹³ tunable light
48 emission,^{14,15} electron-phonon coupling,¹⁶ ferroelectricity,^{17,18} Rashba effect¹⁹ and transfer of
49 chirality.²⁰ However, most of these studies on 2D HaPs have been performed on lower n -values
50 ($n=1, 2$) largely due to difficulties in reproducibly growing higher n -value phase pure crystals and
51 films ($n>2$)^{5,13,21-23}. We hypothesize that the mixed phases (multiple n -values) largely arise from
52 the lack of sufficient control of crystallization kinetics (temperature, time) using the classical
53 synthesis (CS) method for the growth of 2D HaP crystals and powders. Briefly, the CS method
54 used across the perovskite research community involves dissolving all precursors in a solvent at
55 an elevated temperature (230 °C) to achieve a supersaturated solution, followed by rapid
56 crystallization through fast cooling by removing the solution from the hot plate to the ambient.¹⁻
57 ^{3,24} Once the temperature reaches below a certain point where supersaturation is excessive,
58 nucleation will dominate, which results in a large number of small crystals (a few micrometers in
59 size) in a short period of time (5-10 minutes). The fast nucleation due to the fast-cooling (230 °C
60 to 25 °C almost instantaneously) makes it challenging to control the rate of crystallization and can
61 result in the heterogeneous growth of unwanted phases. Therefore, we hypothesize that decoupling
62 the crystallization temperature and time would enable a much better control over the kinetics of
63 growth, which is challenging to achieve using the CS method since there is limited freedom to
64 control the temperature or time one at a time during the crystallization process. As a result,
65 understanding the impact of the kinetic parameters on realizing phase pure 2D perovskites has
66 been largely unexplored and systematic studies on the effect on tuning the temperature or time of

67 crystallization for a given stoichiometry are still missing. In addition to difficulties in achieving
68 phase pure crystals using the CS method, the powder forms of 2D-HaP are limited by their small
69 crystal sizes (μm to mm sizes), making it challenging to precisely analyze the intrinsic physical
70 properties such as (i) Light-matter interactions;²⁵⁻²⁷ (ii) Optical measurement and dielectric
71 functions where large-area flat crystals are required;⁴ (iii) Electron-phonon interactions, where
72 carrier trapping and exciton dissociation at grain boundaries or edges can often lead to complicated
73 spectra.²⁸⁻³⁰

74 Attempts to cultivate large 2D hybrid perovskite (HaP) crystals have been made by slowing
75 down growth through increased crystallization temperature and dilution,^{31,32} but with limited
76 success in achieving higher n -values ($n \geq 4$).^{1,24,30,33-35} Hence, the traditional methods of acquiring
77 high n -value crystals have involved either (i) separating n -pure crystallites from an n -mixed
78 crystal²⁴ or (ii) making several synthesis attempts. Nonetheless, a direct and reliable technique for
79 producing phase-pure high n -value crystals is imperative.

80 Here we demonstrate that by either prolonging the crystallization time at a constant
81 temperature or adjusting the synthesis temperature at a constant crystallization time, the initial 2D-
82 HaP crystal can transform from lower to higher n -values. This transformation was verified through
83 in-situ absorbance and x-ray diffraction measurements. To control the crystallization kinetics, we
84 confined the precursor solution's volume between two glass slides and mounted it on a hot plate to
85 precisely regulate the heating and cooling rates. In-situ photoluminescence spectroscopy and
86 imaging suggest that the transformation from a lower n -value to a higher n -value starts from the
87 edges of the preformed crystals, eventually converting the entire crystal into higher- n 2D-HaP
88 crystals. Based on the experimental data collected from the KCSC method, we created multi-
89 parameter phase diagrams for both the RP and DJ 2D-HaP using machine learning. Finally, we
90 show that the concept of isothermal control can be translated to the CS process used commonly
91 across the research community to synthesize powders of 2D-HaP, which allows us to synthesize
92 2D-HaPs from $n=1-6$. We believe that the direct and reproducible approach method we propose
93 for obtaining phase-pure single crystals and powders can be applied to RP and DJ-based
94 perovskites of varying compositions. This will allow for a broader investigation of the physical
95 properties of these perovskites, which has been previously limited to those with $n=1$ or 2 .

96 Furthermore, these studies may uncover new opportunities for technological applications beyond
97 using these perovskites solely as passivation layers or additives in bulk 3D perovskite films.^{33,36}

98 **1. Result and discussion**

99 **1.1 KCSC method and transformation**

100 The progressive transformation to high n is demonstrated via the KCSC method, which is
101 illustrated in Fig. 1a. To observe the transformation phenomenon, we used a parent solution of low
102 n -value ($n=3$) stoichiometry (mol ratio, Pb: MA: BA=4: 2.67: 1.71) of $\text{BA}_2\text{MA}_{n-1}\text{Pb}_n\text{I}_{3n+1}$ to obtain
103 large-area crystals of high n -values ($n=4-6$) by tuning the crystallization temperature and time.
104 First, same as in CS, all the precursors (PbO, Methylammonium chloride (MACl), and Butylamine
105 (BA)) are dissolved and mixed in the hydroiodic acid with the concentration of 0.85 M (based on
106 Pb) at 190 °C. To prevent supersaturation and promote gradual growth of crystals, the solution is
107 diluted by a factor of two. The diluted solution is then sandwiched between two preheated glass
108 substrates treated with UV-ozone and placed on a hotplate for annealing at varying temperatures.
109 When the substrate is annealed between 55°C and 105°C, a large crystal grows gradually due to
110 limited solvent evaporation at the substrate's edge. Annealing below 55°C or above 105°C is not
111 recommended as evaporation is minimal or the solution boils off, respectively. At a relatively low
112 temperature within this range, the resulting crystal's n value corresponds to the parent solution's
113 stoichiometry. For instance, annealing a parent solution of RP with $n=3$ stoichiometry below 76°C
114 produces a crystal with an n value of 3. Conversely, annealing at a higher temperature between
115 80°C and 105°C leads to the formation of higher n values such as $n=4$ and 5 as the initial crystal.
116 If the temperature is kept constant and the crystal is monitored over time, the initial n value will
117 transform into higher n values, regardless of the starting n -value.

118 We performed in-situ optical absorbance and X-ray spectroscopy measurements on the RP 2D-
119 HaP crystal fabricated by the KCSC method using a parent solution with the stoichiometry of $n=3$,
120 where we tuned the temperature and time separately. For the time-dependent experiment, we
121 increased the time of crystallization at a fixed temperature. For the temperature-dependent
122 experiment, we varied the temperature of synthesis for a fixed crystallization time. Figure 1b
123 illustrates the evolution of optical absorption as a function of temperature (ranging from 60-100 °C)
124 for a fixed time of 7 hours using the same $n=3$ stoichiometry parent solution. At low temperatures

125 (60-66 °C), we observed the formation of the n=3 crystal, which was identified based on the
126 exciton absorption peak at 2.04 eV and also validated by comparison with that of the n=3 single
127 crystal.^{1,4} However, as we increase the temperature further to 68-79 °C, we observe a new peak at
128 1.92 eV, which is redshifted from the n=3 peak. When further increasing the temperature from
129 80 °C to 100 °C, we observed yet another set of peaks emerge at 1.85 eV and 1.8 eV. Evaluation
130 of the peak positions and their comparison with a single crystal of 2D-HaP fabricated using the
131 classical method suggests that these peaks at 1.92 eV, 1.85 eV, and 1.8 eV corresponding to n=4,
132 n=5, and n=6 respectively,^{1,4} which were further validated using x-ray diffraction measurements
133 as shown in Fig. 1c. Briefly, the n=3 crystal is formed at 60 °C indicated by the set of corresponding
134 (0k0) peaks consistent with the n=3 single crystals previously synthesized^{1,4,24}, which upon
135 increasing the temperature to 80 °C, gives rise to (0k0) peaks of n=4 with a concomitant decrease
136 in the intensity of the n=3 peaks. As we further increased the temperature to 100 °C, (0k0) peaks
137 of n=5 appeared and dominated, with the decreasing of the n=4 peaks. The evolution from n=3 to
138 n=4 and finally n=5 observed in x-ray diffraction measurements is consistent with the temperature-
139 dependent absorption measurements.

140 We changed the duration of crystallization at a constant temperature of 75°C and monitored the
141 growth of a single perovskite crystal after every one-hour interval. The absorbance spectra versus
142 time for the KCSC method are displayed in Figure 1d. Initially, n=3 was formed within 4 hours,
143 followed by n=4 after 5 hours, causing the original n=3 excitonic peak intensity to decrease.
144 Heating the crystal further at 75°C resulted in its transformation to n=5 after 13 hours. However,
145 the crystal did not quickly convert from n=5 upon continued annealing, which is expected since
146 the n=6 compound is less thermodynamically favorable.²⁴ The optical absorbance measurements
147 are further supported by time-dependent XRD measurement as shown in Fig. 1e, and Fig. S1,
148 where a n=3 crystal slowly transforms to n=4 after 7 hours of growth and finally to n=5 after 13
149 hours. These measurements clearly show that we can tune the n value progressively by controlling
150 temp and time separately.

151 The lateral size of the crystal fabricated by the KCSC method is a few millimeters to centimeters
152 depending on the growth time. The thickness of the crystals is around 500 nm, which was
153 calibrated to the amount of solution (Fig. S2) and the top glass slide used to confine the solution

154 since the spacing between two substrates could be tuned by varying the pressure applied to the
 155 apparatus.³¹ XRD measurements suggest that the orientation of the crystals are along the stacking

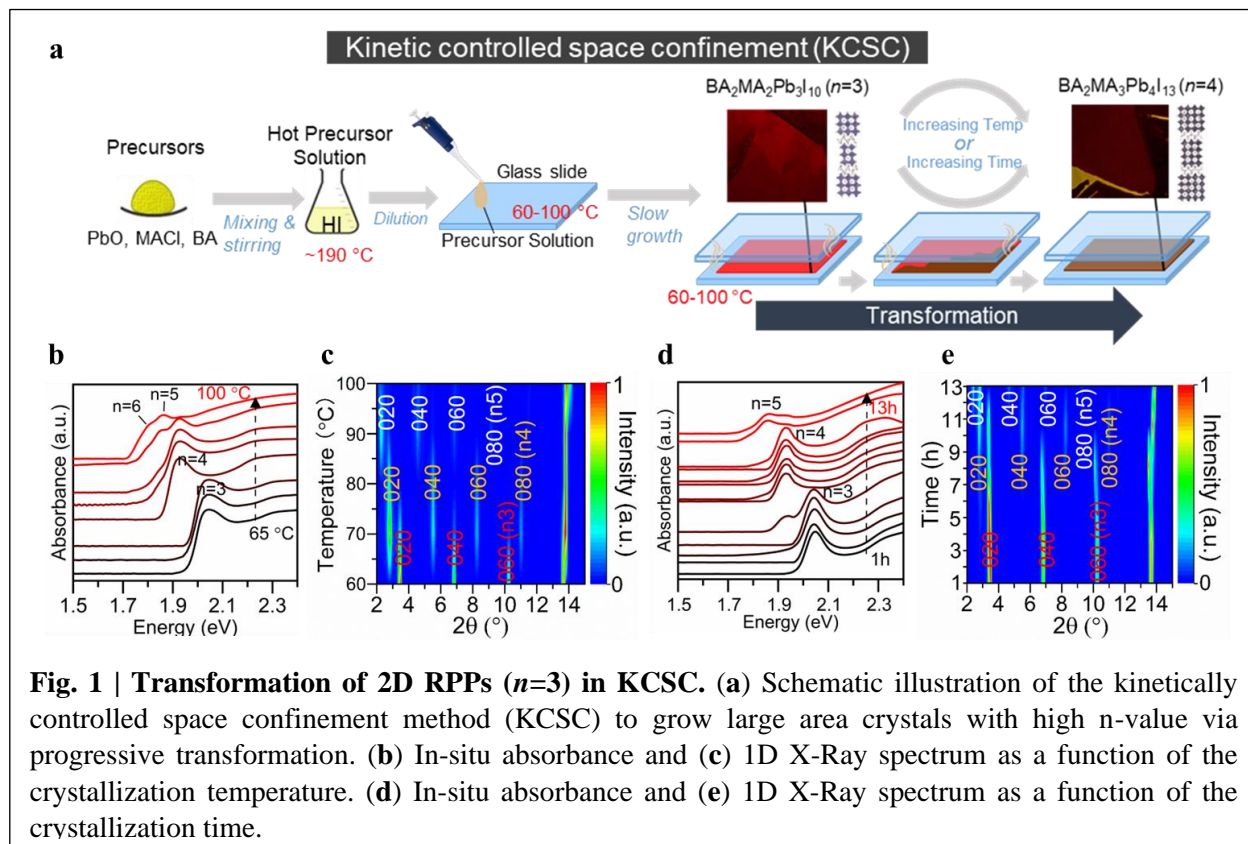


Fig. 1 | Transformation of 2D RPPs ($n=3$) in KCSC. (a) Schematic illustration of the kinetically controlled space confinement method (KCSC) to grow large area crystals with high n -value via progressive transformation. (b) In-situ absorbance and (c) 1D X-Ray spectrum as a function of the crystallization temperature. (d) In-situ absorbance and (e) 1D X-Ray spectrum as a function of the crystallization time.

156 axis (or in-plane) as determined from the characteristic low angle ($0k0$) reflections corresponding
 157 to the lattice constants in the stacking direction (Figure S3) with no detectable signal of (111)
 158 perovskite peak. Experimental Grazing incident wide-angle X-ray (GIWAX) measurements (Fig.
 159 S4) match with simulated indexing of horizontally oriented 2D perovskite structure, indicating the
 160 in-plane orientation of the perovskite layers.³⁶

161 To rationalize the transformation in 2D HaP from a thermodynamics perspective, we calculate
 162 the enthalpy of formation (ΔH) and the Gibbs free energy (ΔG) for the RP 2D-HaP crystal. The
 163 enthalpy of transformation was calculated based on the reaction scheme given in table S1, where
 164 the reactants are a specific n -value crystal, PbI_2 , MAI while the product is the ($n+1$) number
 165 crystal (Fig. S5, Table S3-S5). Since $\Delta G = \Delta H - T(\Delta S)$, for the temperature-dependent
 166 transformation, we have that ΔG is mainly dependent on the ΔH since the change of entropy ΔS is
 167 negligible²⁴. The negative ΔH value of -62.5 KJ/mol for the $n=3$ to $n=4$ transformation indicates
 168 it is favorable. For the transformation of $n=4$ to $n=5$, the ΔH becomes more positive indicating a

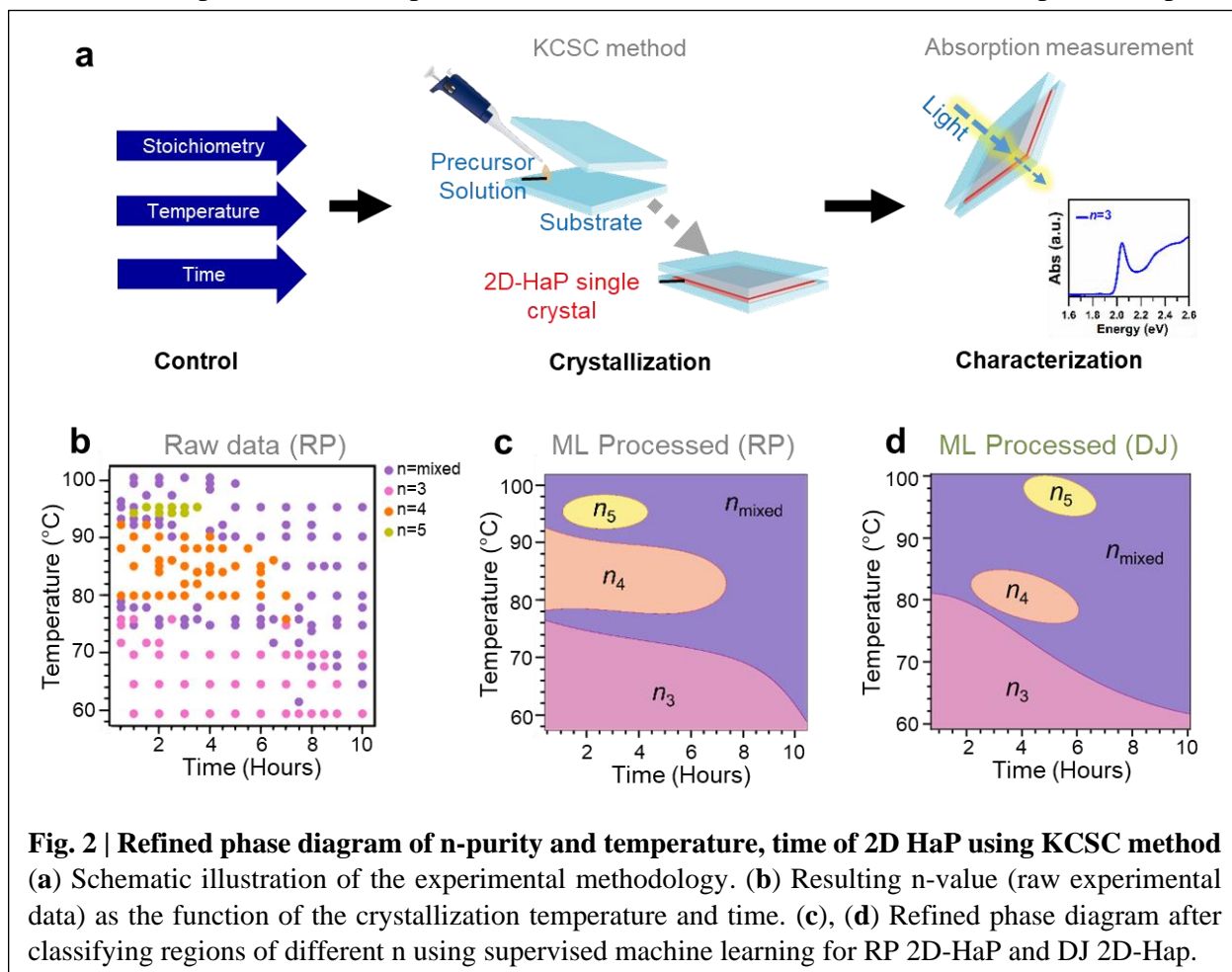
169 low probability of fabricating a phase pure 2D perovskite. Furthermore, the transformation from
170 $n=5$ to $n=6$ is extremely unfavorable because of the high enthalpy of transformation, equaling 149
171 KJ/mol (Table S3). To overcome the large energy barrier, parent solutions of higher n -values
172 ($n=4,5$) were also tested with annealing at high temperature and long time. Higher n -value parent
173 solutions facilitate the formation of higher n -value crystals compared to a $n=3$ solution, but with
174 decreasing reproducibility. For a $n=4$ solution, a $n=4$ crystal is formed at low temperature (below
175 $76\text{ }^{\circ}\text{C}$), while at very high temperature ($105\text{ }^{\circ}\text{C}$) with long annealing time (10 hours) it can form
176 $n=6$ crystal (Fig. S6). For parent solution of $n\geq 5$, a specific n -value can not be obtained and 3D
177 HaP is formed instead since it is more thermodynamically favorable than higher n -value ($\Delta H_f: n=5$
178 $< \text{MAPbI}_3(3\text{D}) < n=6$).²⁴

179 **1.2 Building a multiparameter phase diagram**

180 To get a global view of the transformations and the relationship between phase purity,
181 temperature and time, we designed and performed over 250 KCSC temperature and time-
182 dependent syntheses for both RP and DJ. For DJ syntheses, we chose 3AMP as the organic cation
183 spacer and used the same experimental methodology as used for RP as illustrated in Fig. 2a. Our
184 approach consisted of four steps: (i) synthesizing the crystal using the same parent solution but
185 with varying temperature and time; (ii) performing large area optical absorption measurements on
186 the crystal, analyzing the excitonic absorption peak position to determine the n -value and; (iii)
187 mapping the resulting n -value as the function of the temperature and time parameters; (iv)
188 deploying machine learning (ML) analysis to refine the map and produce the phase diagram with
189 smooth boundaries. Fig. 2b shows the results of the experiment of 2D-HaPs using $n=3$
190 stoichiometry parent solution, each data point represents one synthesis performed at a specific
191 temperature during a given time. We classified them into four categories: the purple points indicate
192 n -mixed phases, the pink data points indicate $n=3$, orange indicates $n=4$, and yellow for $n=5$. The
193 n -mixed phases are defined if the crystal contains more than one n value indicated by the multiple
194 excitonic absorption peaks. However, we find that in some regions there is a large variance of the
195 phase pure and mixed-phase crystals. For example, when synthesizing large area $n=3$ KCSC
196 crystals at $70\text{ }^{\circ}\text{C}$ and >8 hours, the border between phase pure and mixed phases is blurred. Our

197 results show that at 70 °C and 9 hours, the KCSC synthesis produces a mixed phase (Fig. 2b).
 198 However, at the same temperature but 10 hours, the sample is phase-pure $n=3$. To alleviate the
 199 uncertainty in these boundaries, we used supervised machine learning (ML) to statistically classify
 200 regions of pure phase vs mixed phase and to formulate a phase diagram (Fig. 2c). Specifically, we
 201 deployed a support vector machine classifier to find the most optimal hyperplane, which can
 202 separate the 2 classes, for this example $n=3$ and the mixed phase. Details of the ML method can
 203 be found in SI section 1.2.

204 For the RP type (Fig.2b), the crystals are phase-pure $n=3$ irrespective of the annealing time
 205 below 60 °C. As we slightly increase temperature (65 °C) the synthesized crystal at short annealing
 206 times are still phase pure, but at longer annealing times the crystal becomes a mixture of phases
 207 ($n=3$ and $n=4$). This indicates a fixed temperature higher than 65 °C is needed to trigger the
 208 transformation. At a fixed temperature of 77 °C, the phase diagram shows that at all times the
 209 KCSC method produces mixed phases. From 78 °C to 92 °C, the KCSC method produced phase



210 pure n =4 RP 2D-HaP right from the start of the annealing, which indicates that higher temperature
211 will facilitate the formation of a higher n-value crystal, which is consistent with our
212 thermodynamics calculations. As we increase the annealing time, the pure n=4 crystal also
213 transforms into an n-mixed crystal because of intercalation. The pure n=5 crystal was acquired
214 from a few conditions at higher temperatures (95 °C) but a relatively short time window. The phase
215 diagram indicates that the temperature for isothermal transformations, determines the initial n-
216 value and time controls the rate of the transformation.

217 Next, we investigate the DJ 2D-HaP using the same approach. As shown in fig. 2c, an ML-
218 assisted mapping of crystals yielded by the KCSC method using 3-(aminomethyl) piperidinium
219 (3AMP) DJ n=3 solution is plotted. By tuning the temperature and time of crystallization, the same
220 parent n=3 solution formed crystals from n=3 to n=5 with high purity. The mapping of DJ 2D-HaP
221 shows a similar trend compared to RP 2D-HaP, where the n-value increases as temperature and
222 time of crystallization increase. The chances of synthesizing phase-pure crystal decrease with
223 increasing n-value, which is demonstrated by the area decrease of the region area of ascendant-n
224 in the map. Nonetheless, one difference between the RP and DJ phase diagram is: For DJ
225 perovskites, the formation of higher n-values (n=4 and n=5) requires higher temperatures and
226 longer times. This is attributed to the smaller interlayer spacing of DJ and additional interlayer
227 interaction, limiting the precursor diffusion or the proposed intercalation mechanism (vide
228 *infra*).^{2,27,37} In summary, the concept of isothermal control demonstrated for both RP and DJ 2D-
229 HaP series suggests it is generally applicable to all the 2D-HaPs.

230 **1.3 Mechanism of transformation**

231 To understand how the 2D-HaPs transform, we considered several possible pathways. Firstly,
232 we looked at the concentration of the precursor solution and whether the loss of certain organic
233 cations (Butyl Ammonium or aminomethyl pyridinium) during growth at high temperature could
234 cause a change in concentration and thus a change in n value. Secondly, we examined whether the
235 dissolution of lower n-value crystals and recrystallization of higher n-value crystals could
236 contribute to the transformation. Thirdly, we considered the possibility that larger A' cations (such
237 as BA) could escape from the perovskite structure during the transformation from n=3 to n=4-6.
238 Finally, we looked at the idea that intercalation of MA⁺, Pb²⁺, and I⁻ from the crystal edges of the
239 first formed 2D-HaP crystal could increase the perovskite-layer thickness. Initially, we explored

240 the possibility that the change in n value was due to the loss of organic spacer cations during the
241 annealing process, which could alter the proportion of inorganic and organic components and thus
242 change the stoichiometry to form higher n -values. To test this hypothesis, we conducted
243 experiments on RP and DJ perovskites, which contain BA and AMP cations. The BA has a boiling
244 point of 78 °C but AMP is at ~230 °C, which is much higher than our experimental temperature
245 range (60 – 100 °C). The organic spacer would not likely escape faster than other cations (MA^+ ,
246 Pb^{2+} , and I) from the solution, therefore we ruled out this possibility.

247 To test the second, third, and fourth potential-pathways, we set up an in-situ photoluminescence
248 (PL) imaging and PL spectrum during the crystal growth process to visualize the transformation
249 (Fig.3). The PL setup is shown in Fig. 3a, where we measured the emission of the 2D-HaP crystal
250 by exciting the whole region using a mercury vapor lamp with a 532 nm short pass filter mount
251 before the sample. This allowed us to photoexcite and image the photoluminescence from the
252 crystal and collect spectrally resolved information during the transformation from low n to high n
253 value. The PL images were collected by adding a Semrock Razoredge 633nm long pass filter right
254 before the CCD camera. The filter suppresses the emission from the RP $n=3$ perovskite and allows
255 for the detection of the $n=4$ phase. Figure 3c (Fig. S7) illustrates the evolution of the 2D-HaP
256 single crystal as a function of time at 77 °C, the dark red region is $n=3$ and the brighter red region
257 is $n=4$. After the $n=3$ crystal forms, under continuous heating we observe the appearance of the
258 $n=4$ at the edge of the $n=3$ crystal, and then with time, the $n=4$ area expands and gradually converts
259 the whole $n=3$ region to $n=4$. Simultaneously, we also probed the photoluminescence spectra as a
260 function of the growth time as shown in Fig. 3b. The circle illustrated on the PL images (fig. 3c)
261 is the probe region with a laser beam diameter of ~15 μm under a 10x objective. The spectra show
262 a progressive change in emission peak from 630 nm to 650 nm indicating an increase in layer
263 thickness from $n=3$ to $n=4$ which agrees with our hypothesis. In addition, the photoluminescence
264 spectra show no other emissions from different sites, which excludes the possibility of defects and
265 third-phase impurities. Lastly, both PL imaging and PL spectra results indicate that the
266 transformation occurs much faster at the edges than in the bulk. We also probed the PL spectra
267 from the back side of the crystal and the identical n was observed (fig.3d), which excluded the
268 possibility that transformation is from a high n -value crystal forming on top of a lower n -value to
269 form vertically stacked heterostructures.

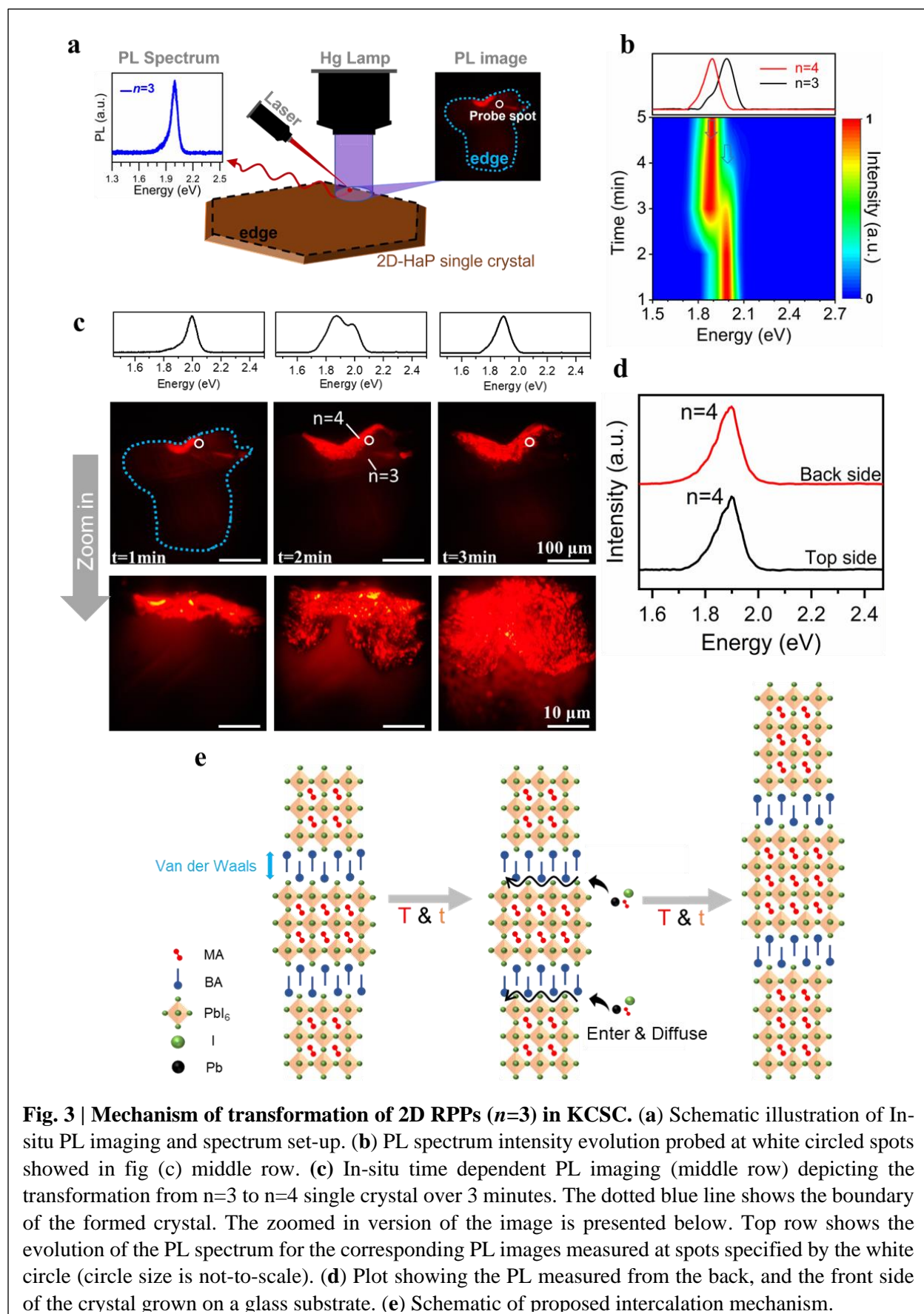


Fig. 3 | Mechanism of transformation of 2D RPPs ($n=3$) in KCSC. (a) Schematic illustration of In-situ PL imaging and spectrum set-up. (b) PL spectrum intensity evolution probed at white circled spots showed in fig (c) middle row. (c) In-situ time dependent PL imaging (middle row) depicting the transformation from $n=3$ to $n=4$ single crystal over 3 minutes. The dotted blue line shows the boundary of the formed crystal. The zoomed in version of the image is presented below. Top row shows the evolution of the PL spectrum for the corresponding PL images measured at spots specified by the white circle (circle size is not-to-scale). (d) Plot showing the PL measured from the back, and the front side of the crystal grown on a glass substrate. (e) Schematic of proposed intercalation mechanism.

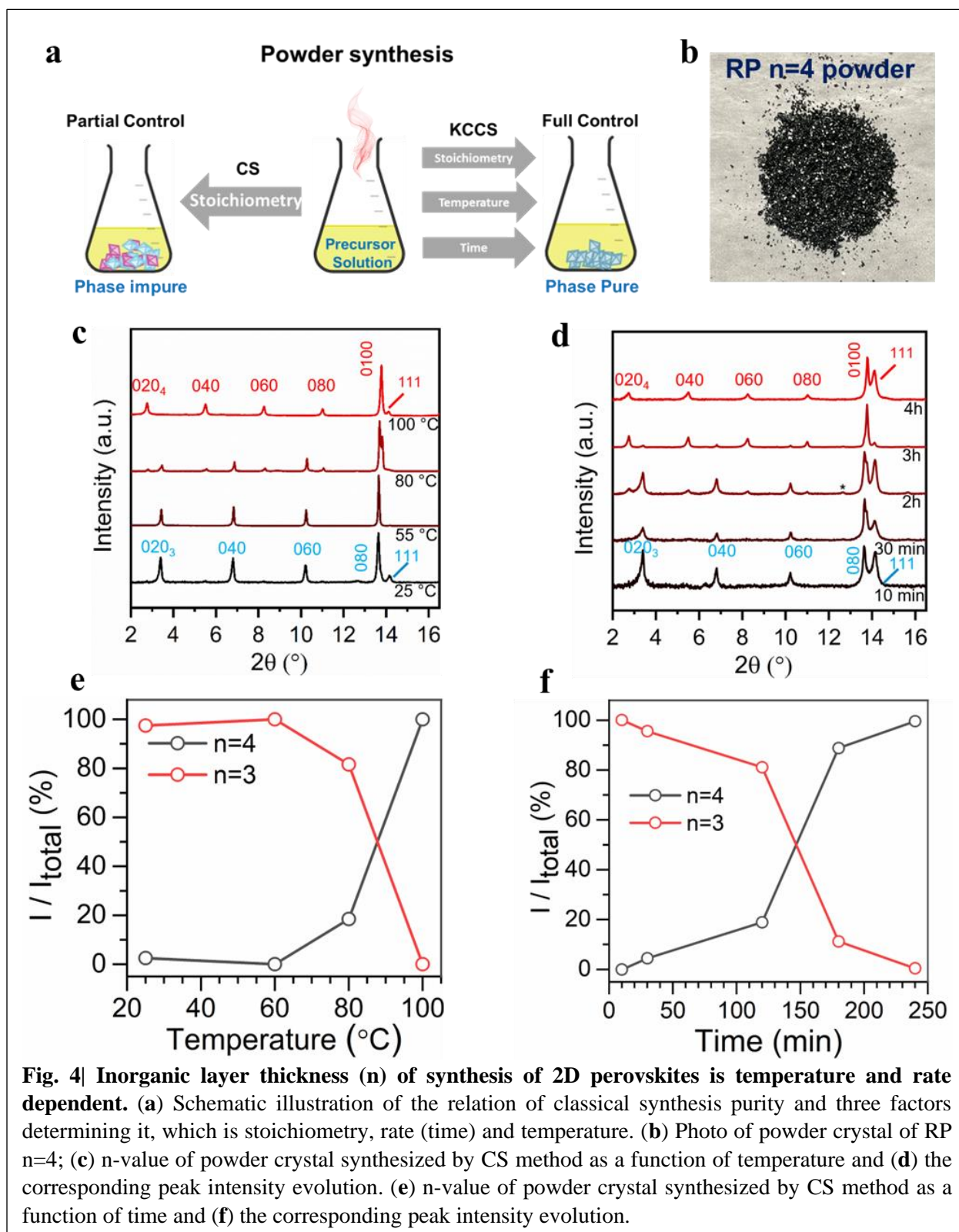
271 Therefore, the second mechanistic hypothesis is also excluded since the transformation occurs
272 without dissolving the $n=3$ and recrystallization of $n=4$. The third hypothesis was excluded after
273 comparing our observations with a previous report by Fang et al.,³⁸ wherein a PL quenching (PL
274 intensity decay) occurred after the 2-phenyl ethyl ammonium (another organic cation forming RP
275 2D-HaP) left the perovskite framework due to laser-induced degradation. However, this is not the
276 case observed in our PL experiments discussed in fig.3, where emissions from higher n emerged
277 without a decrease in PL intensity.

278 Finally, we propose that the transformation is through an intercalation process, where small
279 precursor ions, such as MA^+ , Pb^{2+} , and I^- penetrate the lattice from the edges of the 2D-HaP crystal
280 and diffuse along the interface between the perovskite layers. These ions fill the voids of the
281 corner-sharing PbI_6 structure, forming additional linkages and integrate with the $[\text{Pb}_n\text{I}_{3n+1}]$ lattice.
282 This templating effect occurs because of the weak ionic interactions between the 2D inorganic
283 octahedral sheets and the organic spacers. Figure 3e illustrates the proposed intercalation growth
284 mechanism for the RP-HaP. Here, in the solution, the $n=3$ perovskite forms first, which are shown
285 by the stacking of 3 inorganic $[\text{Pb}_n\text{I}_{3n+1}]^{(n+1)-}$ layers separated by the butylammonium organic
286 spacer cations. Then over time, the organic MA, Pb, and I molecules diffuse through the edges of
287 the $n=3$ 2D-HaP crystal and attach to the $[\text{Pb}_n\text{I}_{3n+1}]$ structure. The intercalation process results in
288 the increase of the layer thickness from $n=3$ to $n=4$ for the synthesized 2D-HaP. This mechanism
289 also explains the observation that DJ HaP requires higher temperature and longer time for
290 transformation because of the extra H-bond between spacer cation and octahedral in DJ HaP,
291 slowing down the intercalation. Our results are consistent with previous reports that observe the
292 intercalation of precursor ions into the lattice to form 2D-HaP and higher layer thickness 2D-HaP.
293 For e. g., Guo et al.³⁹ proposed that extra halide additives (K^+) would facilitate the intercalation
294 of PbBr_6^{4-} octahedra into the lower- n $\text{PEA}_2\text{FA}_{n-1}\text{Pb}_n\text{Br}_{3n+1}$ (PEA = phenylethylamine, FA =
295 formamidine) to transform to higher n which is associated with Coulomb interaction.

296 **1.4 Applying the KCSC to the classical method for batch-scale synthesis of 2D-HaPs powders**

297 While the KCSC method provides excellent control over phase pure, large area high n -value
298 ($n=1-6$) monocrystals of 2D-HaP, it is not scalable. As a result, with the goal of using the crystal
299 transformation principle to achieve phase pure crystals in large quantities, we investigated the
300 effects of controlling the temperature and time using a modified classical synthesis (CS) approach.

301 Figure 4a illustrates the CS method process, in which all the precursors are mixed in a concentrated
 302 hydriodic acid (HI) at a specific stoichiometric ratio according to the target n-value. The solution
 303 is heated to boiling and rapidly cooled to room temperature within 1 hour or even shorter period.



304 Small flakes with a typical lateral size of around 100 μm were obtained. However, polycrystalline
305 samples produced from this CS method often contain mixtures of different n -values. For example,
306 Fig. S8a shows the X-ray diffraction pattern for 10 classically synthesized $n=3$ RP samples, in
307 which only 7 of the 10 syntheses achieved were phase-pure. The diffraction patterns of the
308 unsuccessful synthesis show a consistent mixture of $n=3$ and $n=4$ phase (RP). Then we transposed
309 the methodology developed in section 1.3 to the CS method. To ensure a uniform temperature
310 across the precursor solution and also a prolonged cooling period, we immersed the reaction vial
311 into an oil bath. The first parameter to tune is the temperature at which the boiling solution is left
312 to crystallize. Instead of room temperature, we test a series of isothermal transformations, figure
313 4c shows the powder X-ray diffraction of 2D-HaP powder crystals synthesized from 25 $^{\circ}\text{C}$ to
314 100 $^{\circ}\text{C}$. It shows a similar temperature dependent trend as observed in the KCSC method. Below
315 60 $^{\circ}\text{C}$ the $n=3$ forms but as the temperature is increased, the resulting powder becomes $n=3$ and
316 $n=4$ mixture at around 80 $^{\circ}\text{C}$ and finally pure $n=4$ at 100 $^{\circ}\text{C}$. However, as we showed in Fig. S8,
317 compared to room temperature, crystallization at 55 $^{\circ}\text{C}$ has a higher probability to obtain pure
318 crystal, which is consistent with the previous discussion in which fast precipitation of the 2D
319 perovskite crystals results in mixed phases.⁴⁰ Our findings suggest that a temperature range of 40-
320 55 $^{\circ}\text{C}$ is essential for the consistent and pure production of 2D-HaP. Within this range, we are able
321 to slow down the crystallization process without inducing any changes caused by higher
322 temperatures. This highlights that the temperature at which the solution is cooled is just as
323 important as stoichiometry in the traditional synthesis method. Next, we also explored the impact
324 of varying the total duration of the crystallization process. Figure 4d illustrates the X-ray
325 diffraction patterns for various crystallization times with the temperature set to 90 $^{\circ}\text{C}$. The results
326 show a trend similar to the KCSC in which, as the time increases, the crystal transitions from $n=3$
327 into a mixture of $n=3$ and $n=4$ and finally phase pure $n=4$ after 4 hours. Figure 4e and 4f are the
328 intensity changes of the corresponding temperature and time-dependent XRD patterns, both of
329 them show that $n=3$ completely converts to $n=4$. The temperature and time-dependent observations
330 we have made clearly demonstrate that stoichiometry is not the sole determinant of the n -value in
331 powder 2D-HaP. Precise control over all three parameters is crucial for the production of a single
332 n -value 2D-HaP. As a result, we propose a new synthesis method called Kinetics-controlled classic
333 synthesis (KCCS) that emphasizes the importance of the control of these parameters in powder
334 synthesis.

335 **1.5 Phase pure n=1 to n=6 of RP and DJ 2D-HaPs**

336 Having established the importance of progressive transformation, we are able to grow phase pure
337 single crystals ranging from n=1 to n=6 for both RP and DJ 2D-HaP. Figure 5a, 5b shows the
338 absorption, and photoluminescence spectrum of KCSC produced n=1 to n=6 RP 2D-HaP single
339 crystal. Each of the KCSC fabricated crystals exhibit a single narrow absorption peak decreasing
340 from 2.42eV to 1.78eV as a function of n value (n=6 to n=1). The photoluminescence emission
341 peak also follows this trend from 2.38eV to 1.77eV. This behavior is consistent with their quantum
342 and dielectric confinement effects⁴¹ and furthermore, indicates the phase purity of the fabricated
343 crystals⁴. Both absorption and PL indicate the high purity of the crystal synthesized by our method.
344 The absorption and photoluminescence of a control MAPbI₃ 3D-HaP are shown in the black curve

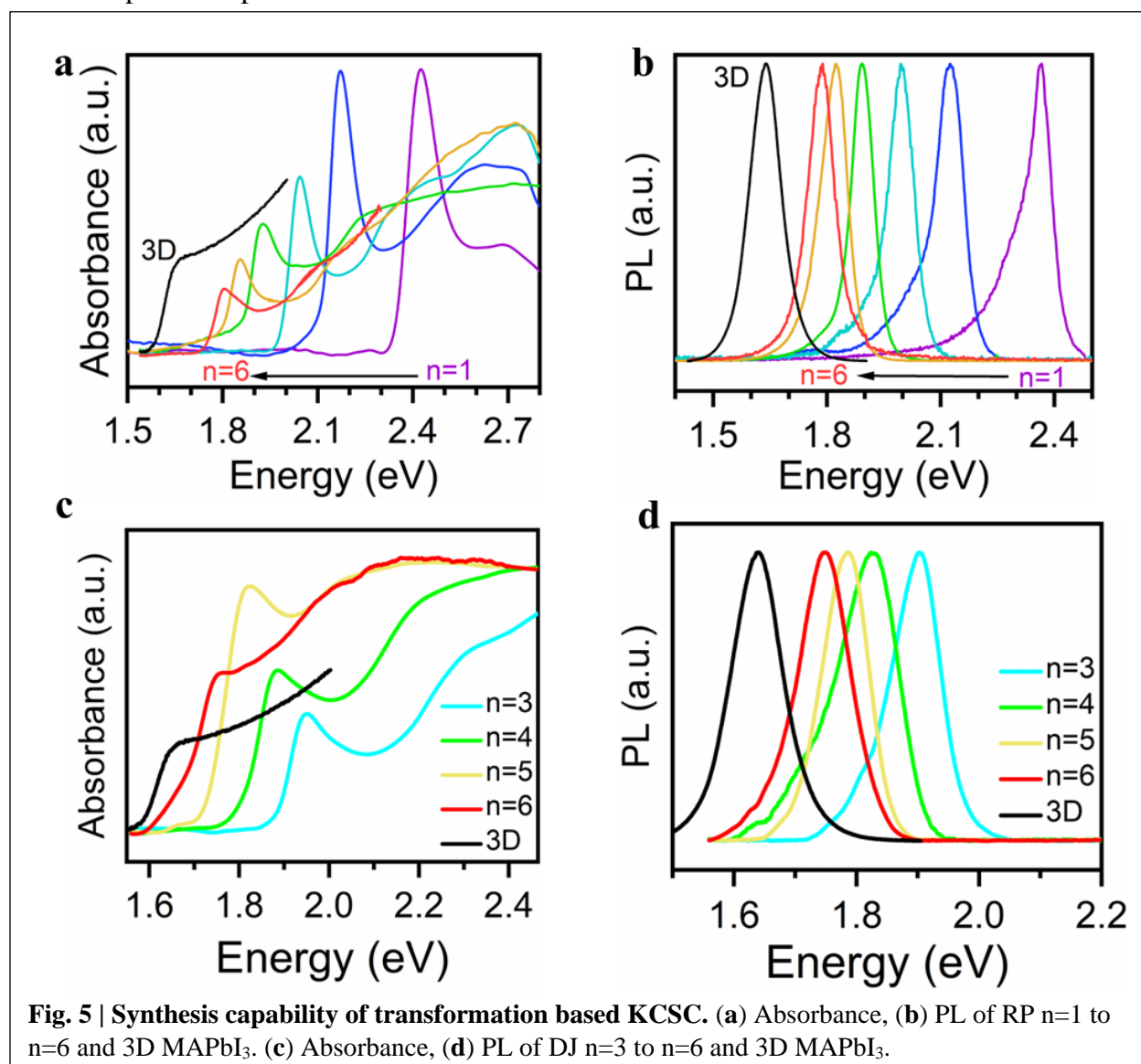


Fig. 5 | Synthesis capability of transformation based KCSC. (a) Absorbance, (b) PL of RP n=1 to n=6 and 3D MAPbI₃. (c) Absorbance, (d) PL of DJ n=3 to n=6 and 3D MAPbI₃.

345 on both plots. X-Ray diffraction of KCSC fabricated crystal (Fig. S9) also shows high purity.
346 Figure 5c, d shows the absorption, and photoluminescence spectrum of KCSC produced n=3 to
347 n=6 DJ 2D-HaP single crystal. Absorption (fig.5c) shows the 3AMP follows the general trend for
348 2D-HaP where the band gap decreases as n increases (1.95eV for n=3, 1.88eV for n=4, 1.82eV for
349 n=5, 1.75eV for n=6). Steady-state photoluminescence (PL) shows an identical trend with the band
350 gaps (1.90eV for n=3, 1.82eV for n=4, 1.79eV for n=5, 1.75eV for n=6). Similar to the 2D-HaP
351 synthesized from KCSC and transformation, the DJ 2D-HaP synthesized by the same approach is
352 of high purity. The band gap of the DJ 3AMP series is smaller than the RP BA series, consistent
353 with previous reports.^{2,37,42} Transformation of the 4-(aminomethyl)piperidinium (4AMP) 2D-HaP
354 is shown in Fig. S10.

355 2. Methods

356 2.1 Crystal synthesis

357 **2.1.1 Reagents:** PbO (99.9%), Methylammonium chloride (MACl, 99.0%), Butylamine (BA,
358 99.0%), 4-(aminomethyl)piperidine (4AMP, 96%), hydroiodic acid (HI, 57 wt % in H₂O, distilled,
359 stabilized, 99.95%), hypophosphorous acid solution (H₃PO₂, 50 wt % in H₂O) and diethyl ether
360 ((C₂H₅)₂O, 98%, contains 2% ethanol and ~10ppm BHT) were purchased from Sigma-Aldrich. 3-
361 (aminomethyl)piperidine (3AMP, 98%) was purchased from TCI, Methylammonium iodide
362 (MAI) were purchased from Greatcellsolar. All chemicals were used as received.

363

364 **2.1.2 Synthesis of (BA)₂(MA)_{n-1}Pb_nI_{3n+1} KCSC parent solution and powder crystal:** RP
365 perovskites solution were synthesized by modifying the previously reported procedure¹. For n =
366 1, PbO powder (892.8 mg, 4mmol) was dissolved in a mixture of 57% w/w aqueous HI solution
367 (4.0 mL, 30.4 mmol) and 50% aqueous H₃PO₂ (1.0 mL, 9.1 mmol) at room temperature (25 °C)
368 under constant magnetic stirring for 10 mins, which formed a bright yellow solution. In a separate
369 beaker, n-CH₃(CH₂)₃NH₂ (369.6 μL, 4 mmol) was neutralized with HI 57% w/w (2 mL, 15.2
370 mmol) in an ice bath resulting in a clear yellow solution. The addition of the n-CH₃(CH₂)₃NH₃I
371 solution to the PbI₂ solution initially produced orange precipitates, which were slowly dissolved
372 under heating the combined solution to boiling. The solution was then diluted 3 times by aqueous
373 HI solution. For higher n, PbO powder (892.8 mg, 4mmol) was dissolved in a mixture of 57% w/w
374 aqueous HI solution (4.0 mL, 30.4 mmol) and 50% aqueous H₃PO₂ (1mL, 9.1 mL) at room

375 temperature (25 °C) under constant magnetic stirring for 5 mins, which formed a bright yellow
376 solution. Subsequent addition of solid $\text{CH}_3\text{NH}_3\text{Cl}$ [135.2 mg, 2 mmol (n=2); 180 mg, 2.67 mmol
377 (n=3); 202.8 mg, 3 mmol (n=4); 216 mg, 3.2 mmol (n=5)] at 230 °C initially caused the
378 precipitation of black powders, which rapidly dissolved under stirring to afford a clear yellow
379 solution. In a separate beaker, n- $\text{CH}_3(\text{CH}_2)\text{NH}_2$ [288 μL , 2.9 mmol (n=2); 170 μL , 1.71 mmol
380 (n=3); 108.8 μL , 1.1 mmol (n=4); 88 μL , 0.89 mmol (n=5)] was neutralized with HI (2 mL, 15.2
381 mmol) in an ice bath resulting in a clear yellow solution. After adding the n- $\text{CH}_3(\text{CH}_2)_3\text{NH}_3\text{I}$
382 solution to the PbI_2 solution, the combined solution was kept at 230 °C, boiling for 10 mins. The
383 solution was taken out and diluted 2 times with aqueous HI solution to afford a yellow clear
384 solution, as the parent solution for the KCSC method.

385
386 **2.1.3 Synthesis of (3AMP)(MA)₂Pb₃I₁₀ KCSC parent solution:** DJ perovskites solution were
387 synthesized by modifying the stoichiometry reported in the 3-(aminomethyl)pyridinium (3AMPY)
388 2D perovskites procedure.³⁷ The KCSC parent solution was diluted 3 times with aqueous HI
389 solution and heated to 150 °C to ensure no crystals precipitated out before used to grow KCSC.

390
391 **2.1.4 Growth of RP KCSC:** Glass (quartz, sapphire could also be used) was used as the substrate
392 for the 2D perovskite growth. Glass substrates were cut into 1-inch* 1-inch squares, cleaned in
393 soap water, acetone, isopropanol by ultrasonication for 20 min each; then dried by argon. The
394 substrates were transferred into a UV-Ozone cleaner, cleaned for 10 mins. The substrates were put
395 on a hot plate, 10 μL of the parent solution was dropped onto the glass surface, another glass was
396 put on top to fully cover the bottom glass and annealed. For n=1 large single crystal, n=1 parent
397 solution is annealed at 70 °C for 6 hours. For n=2 large single crystal, n=2 parent solution is
398 annealed at 70 °C for 6 hours. For n=3 large single crystal, n=3 parent solution is annealed at 60 °C
399 for 5 hours. For n=4 large single crystal, n=3 parent solution is annealed at 80 °C for 6 hours. For
400 n=5 large single crystal, n=3 parent solution is annealed at 95 °C for 4 hours. For n=6 large single
401 crystal, n=4 parent solution is annealed at 105 °C for 10 hours. Then the top glass is removed, the
402 crystal with the bottom glass is placed on spin coater, 40 μL *3 of the diethyl ether was dropped
403 instantly and spin coated at 3000 r.p.m for 30 seconds followed by heating for 15 minutes to
404 remove all the residue parent solution.

405

406 **2.1.5 Growth of DJ KCSC:** For DJ phase, a growth procedure similar to BA was used with
407 adjustment of temperature and time. For n=3 large single crystal, n=3 parent solution is annealed
408 at 60 °C for 6 hours. For n=4 large single crystal, n=3 parent solution is annealed at 80 °C for 5
409 hours. For n=5 large single crystal, n=3 parent solution is annealed at 96 °C for 6.5 hours. For n=6
410 large single crystal, n=4 parent solution is annealed at 105 °C for 10 hours.

411

412 **2.2 X-ray diffraction measurements**

413 The measurements were conducted using a Rigaku Smartlab X-Ray diffractometer with Cu(K α)
414 radiation ($\lambda = 1.5406 \text{ \AA}$). For each KCSC sample, it was measured right after removing the top
415 glass and washing the crystal, with a step of 0.03° and a speed of 3 degrees per minute. For the
416 powder crystal, it dried in a vacuum oven at 65 °C overnight before measurement.

417

418 **2.3 Grazing incidence wide angle x-ray scattering (GIWAXS)**

419 The GIWAXS diffraction spectra used in this paper were high-resolution synchrotron patterns
420 measured at 11-BM at the National Synchrotron Light Source-II (NSLS II). At beamline 11-BM,
421 samples were placed on a robotic stage inside a vacuum chamber 6 (10⁻² torr) with the sample
422 267mm away from a Pilatus 800K (Dectris) area detector. The photon energy was 13.5 keV, and
423 the beam size was 200 $\mu\text{m} \times 50 \mu\text{m}$ (H \times V).

424

425 **2.4 In-situ absorbance measurements**

426 The optical absorbance measurements were conducted using a broad-band light source (Thorlabs
427 Solis-3C) focused onto the sample with a 50 μm beam size. The transmitted spectrum was collected
428 by optical fiber and then sent to the spectrometer (Andor Kymera 328i) and CCD (Andor iDus
429 416). The measurement was conducted on the KCSC apparatus without removing the top glass.

430

431 **2.5 In-situ PL imaging and spectrum measurements**

432 The in-situ PL imaging was conducted based on a lab-built widefield microscope using a Mercury
433 light source (Olympus U-LH100HG) for illumination source which was loosely focused onto the
434 sample on the hot plate. The PL was spectrally filtered by a long-pass filter (BLP01-647R,
435 Semrock) to selectively monitor the emission from RP BA n=4 crystal, and the PL images were
436 monitored as time lapses recorded by a microscope camera (AmScope MU500). The in-situ PL

437 spectrum was collected on the same area by focusing a 543.5nm Helium-Neon Laser onto a 15 μ m
438 spot within the field of view of the PL image and was monitored by CCD spectrometer (Thorlabs
439 CCS200). Both PL imaging and PL setup were interchangeable without repositioning the samples,
440 allowing for spatially and spectrally-resolved in-situ PL tracing. Both measurements were
441 conducted on the KCSC apparatus without removing the top glass.

442

443 References

- 444 (1) Stoumpos, C. C.; Cao, D. H.; Clark, D. J.; Young, J.; Rondinelli, J. M.; Jang, J. I.; Hupp, J. T.;
445 Kanatzidis, M. G. Ruddlesden–Popper Hybrid Lead Iodide Perovskite 2D Homologous
446 Semiconductors. *Chem. Mater.* **2016**, *28* (8), 2852–2867.
447 <https://doi.org/10.1021/acs.chemmater.6b00847>.
- 448 (2) Mao, L.; Ke, W.; Pedesseau, L.; Wu, Y.; Katan, C.; Even, J.; Wasielewski, M. R.; Stoumpos, C.
449 C.; Kanatzidis, M. G. Hybrid Dion–Jacobson 2D Lead Iodide Perovskites. *J. Am. Chem. Soc.*
450 **2018**, *140* (10), 3775–3783. <https://doi.org/10.1021/jacs.8b00542>.
- 451 (3) Soe, C. M. M.; Stoumpos, C. C.; Kepenekian, M.; Traoré, B.; Tsai, H.; Nie, W.; Wang, B.; Katan,
452 C.; Seshadri, R.; Mohite, A. D.; Even, J.; Marks, T. J.; Kanatzidis, M. G. New Type of 2D
453 Perovskites with Alternating Cations in the Interlayer Space, $(\text{C}(\text{NH}_2)_3)(\text{CH}_3\text{NH}_3)_n\text{Pb}_n\text{I}_{3n}$
454 $_{+1}$: Structure, Properties, and Photovoltaic Performance. *J. Am. Chem. Soc.* **2017**, *139* (45),
455 16297–16309. <https://doi.org/10.1021/jacs.7b09096>.
- 456 (4) Song, B.; Hou, J.; Wang, H.; Sidhik, S.; Miao, J.; Gu, H.; Zhang, H.; Liu, S.; Fakhraai, Z.; Even,
457 J.; Blancon, J.-C.; Mohite, A. D.; Jariwala, D. Determination of Dielectric Functions and Exciton
458 Oscillator Strength of Two-Dimensional Hybrid Perovskites. *ACS Mater. Lett.* **2021**, *3* (1), 148–
459 159. <https://doi.org/10.1021/acsmaterialslett.0c00505>.
- 460 (5) Dou, L.; Wong, A. B.; Yu, Y.; Lai, M.; Kornienko, N.; Eaton, S. W.; Fu, A.; Bischak, C. G.; Ma,
461 J.; Ding, T.; Ginsberg, N. S.; Wang, L.-W.; Alivisatos, A. P.; Yang, P. Atomically Thin Two-
462 Dimensional Organic-Inorganic Hybrid Perovskites. *Science* **2015**, *349* (6255), 1518–1521.
463 <https://doi.org/10.1126/science.aac7660>.
- 464 (6) Bao, Z.; Dodabalapur, A.; Lovinger, A. J. Soluble and Processable Regioregular Poly (3-
465 hexylthiophene) for Thin Film Field-effect Transistor Applications with High Mobility. *Appl.*
466 *Phys. Lett.* **1996**, *69* (26), 4108–4110.
- 467 (7) Mannsfeld, S. C.; Tee, B. C.; Stoltenberg, R. M.; Chen, C. V.; Barman, S.; Muir, B. V.; Sokolov,
468 A. N.; Reese, C.; Bao, Z. Highly Sensitive Flexible Pressure Sensors with Microstructured Rubber
469 Dielectric Layers. *Nat. Mater.* **2010**, *9* (10), 859–864.
- 470 (8) Kim, H.-S.; Lee, C.-R.; Im, J.-H.; Lee, K.-B.; Moehl, T.; Marchioro, A.; Moon, S.-J.; Humphry-
471 Baker, R.; Yum, J.-H.; Moser, J. E. Lead Iodide Perovskite Sensitized All-Solid-State Submicron
472 Thin Film Mesoscopic Solar Cell with Efficiency Exceeding 9%. *Sci. Rep.* **2012**, *2* (1), 1–7.
- 473 (9) Burschka, J.; Pellet, N.; Moon, S.-J.; Humphry-Baker, R.; Gao, P.; Nazeeruddin, M. K.; Grätzel,
474 M. Sequential Deposition as a Route to High-Performance Perovskite-Sensitized Solar Cells.
475 *Nature* **2013**, *499* (7458), 316–319.
- 476 (10) Blancon, J.-C.; Even, J.; Stoumpos, Costas. C.; Kanatzidis, Mercouri. G.; Mohite, A. D.
477 Semiconductor Physics of Organic–Inorganic 2D Halide Perovskites. *Nat. Nanotechnol.* **2020**, *15*
478 (12), 969–985. <https://doi.org/10.1038/s41565-020-00811-1>.
- 479 (11) Ghosh, D.; Acharya, D.; Pedesseau, L.; Katan, C.; Even, J.; Tretiak, S.; Neukirch, A. J. Charge
480 Carrier Dynamics in Two-Dimensional Hybrid Perovskites: Dion–Jacobson vs. Ruddlesden–
481 Popper Phases. *J. Mater. Chem. A* **2020**, *8* (42), 22009–22022.
482 <https://doi.org/10.1039/D0TA07205B>.

- 483 (12) Milot, R. L.; Sutton, R. J.; Eperon, G. E.; Haghighirad, A. A.; Martinez Hardigree, J.; Miranda, L.;
484 Snaith, H. J.; Johnston, M. B.; Herz, L. M. Charge-Carrier Dynamics in 2D Hybrid Metal–Halide
485 Perovskites. *Nano Lett.* **2016**, *16* (11), 7001–7007. <https://doi.org/10.1021/acs.nanolett.6b03114>.
- 486 (13) Li, P.; Chen, Y.; Yang, T.; Wang, Z.; Lin, H.; Xu, Y.; Li, L.; Mu, H.; Shivananju, B. N.; Zhang, Y.
487 Two-Dimensional CH₃NH₃PbI₃ Perovskite Nanosheets for Ultrafast Pulsed Fiber Lasers. *ACS*
488 *Appl. Mater. Interfaces* **2017**, *9* (14), 12759–12765.
- 489 (14) Xing, J.; Zhao, Y.; Askerka, M.; Quan, L. N.; Gong, X.; Zhao, W.; Zhao, J.; Tan, H.; Long, G.;
490 Gao, L.; Yang, Z.; Voznyy, O.; Tang, J.; Lu, Z.-H.; Xiong, Q.; Sargent, E. H. Color-Stable Highly
491 Luminescent Sky-Blue Perovskite Light-Emitting Diodes. *Nat. Commun.* **2018**, *9* (1), 3541.
492 <https://doi.org/10.1038/s41467-018-05909-8>.
- 493 (15) Zhao, B.; Bai, S.; Kim, V.; Lamboll, R.; Shivanna, R.; Auras, F.; Richter, J. M.; Yang, L.; Dai, L.;
494 Alsari, M.; She, X.-J.; Liang, L.; Zhang, J.; Lilliu, S.; Gao, P.; Snaith, H. J.; Wang, J.; Greenham,
495 N. C.; Friend, R. H.; Di, D. High-Efficiency Perovskite–Polymer Bulk Heterostructure Light-
496 Emitting Diodes. *Nat. Photonics* **2018**, *12* (12), 783–789. [https://doi.org/10.1038/s41566-018-](https://doi.org/10.1038/s41566-018-0283-4)
497 0283-4.
- 498 (16) Gong, X.; Voznyy, O.; Jain, A.; Liu, W.; Sabatini, R.; Piontkowski, Z.; Walters, G.; Bappi, G.;
499 Nokhrin, S.; Bushuyev, O. Electron–Phonon Interaction in Efficient Perovskite Blue Emitters. *Nat.*
500 *Mater.* **2018**, *17* (6), 550–556.
- 501 (17) Shi, C.; Ye, L.; Gong, Z.-X.; Ma, J.-J.; Wang, Q.-W.; Jiang, J.-Y.; Hua, M.-M.; Wang, C.-F.; Yu,
502 H.; Zhang, Y.; Ye, H.-Y. Two-Dimensional Organic–Inorganic Hybrid Rare-Earth Double
503 Perovskite Ferroelectrics. *J. Am. Chem. Soc.* **2020**, *142* (1), 545–551.
504 <https://doi.org/10.1021/jacs.9b11697>.
- 505 (18) Liu, Y.; Han, S.; Wang, J.; Ma, Y.; Guo, W.; Huang, X.-Y.; Luo, J.-H.; Hong, M.; Sun, Z. Spacer
506 Cation Alloying of a Homoconformational Carboxylate *Trans* Isomer to Boost in-Plane
507 Ferroelectricity in a 2D Hybrid Perovskite. *J. Am. Chem. Soc.* **2021**, *143* (4), 2130–2137.
508 <https://doi.org/10.1021/jacs.0c12513>.
- 509 (19) Zhai, Y.; Baniya, S.; Zhang, C.; Li, J.; Haney, P.; Sheng, C.-X.; Ehrenfreund, E.; Vardeny, Z. V.
510 Giant Rashba Splitting in 2D Organic-Inorganic Halide Perovskites Measured by Transient
511 Spectroscopies. *Sci. Adv.* **2017**, *3* (7), e1700704. <https://doi.org/10.1126/sciadv.1700704>.
- 512 (20) Huang, P.-J.; Taniguchi, K.; Miyasaka, H. Bulk Photovoltaic Effect in a Pair of Chiral–Polar
513 Layered Perovskite-Type Lead Iodides Altered by Chirality of Organic Cations. *J. Am. Chem. Soc.*
514 **2019**, *141* (37), 14520–14523.
- 515 (21) Fieramosca, A.; De Marco, L.; Passoni, M.; Polimeno, L.; Rizzo, A.; Rosa, B. L. T.; Cruciani, G.;
516 Dominici, L.; De Giorgi, M.; Gigli, G.; Andreani, L. C.; Gerace, D.; Ballarini, D.; Sanvitto, D.
517 Tunable Out-of-Plane Excitons in 2D Single-Crystal Perovskites. *ACS Photonics* **2018**, *5* (10),
518 4179–4185. <https://doi.org/10.1021/acsphotonics.8b00984>.
- 519 (22) Wang, J.; Li, J.; Lan, S.; Fang, C.; Shen, H.; Xiong, Q.; Li, D. Controllable Growth of Centimeter-
520 Sized 2D Perovskite Heterostructures for Highly Narrow Dual-Band Photodetectors. *ACS Nano*
521 **2019**, *12*.
- 522 (23) Wang, K.; Wu, C.; Yang, D.; Jiang, Y.; Priya, S. Quasi-Two-Dimensional Halide Perovskite
523 Single Crystal Photodetector. *ACS Nano* **2018**, *12* (5), 4919–4929.
524 <https://doi.org/10.1021/acsnano.8b01999>.
- 525 (24) Soe, C. M. M.; Nagabhushana, G. P.; Shivaramaiah, R.; Tsai, H.; Nie, W.; Blancon, J.-C.;
526 Melkonyan, F.; Cao, D. H.; Traoré, B.; Pedesseau, L.; Kepenekian, M.; Katan, C.; Even, J.; Marks,
527 T. J.; Navrotsky, A.; Mohite, A. D.; Stoumpos, C. C.; Kanatzidis, M. G. Structural and
528 Thermodynamic Limits of Layer Thickness in 2D Halide Perovskites. *Proc. Natl. Acad. Sci.* **2019**,
529 *116* (1), 58–66. <https://doi.org/10.1073/pnas.1811006115>.
- 530 (25) Singh, A.; Lynch, J.; Anantharaman, S. B.; Hou, J.; Singh, S.; Kim, G.; Mohite, A. D.; Singh, R.;
531 Jariwala, D. Cavity-Enhanced Raman Scattering from 2D Hybrid Perovskites. *J. Phys. Chem. C*
532 **2022**, *126* (27), 11158–11164. <https://doi.org/10.1021/acs.jpcc.2c01577>.

- 533 (26) Anantharaman, S. B.; Stevens, C. E.; Lynch, J.; Song, B.; Hou, J.; Zhang, H.; Jo, K.; Kumar, P.;
534 Blancon, J.-C.; Mohite, A. D.; Hendrickson, J. R.; Jariwala, D. Self-Hybridized Polaritonic
535 Emission from Layered Perovskites. *Nano Lett.* **2021**, *21* (14), 6245–6252.
536 <https://doi.org/10.1021/acs.nanolett.1c02058>.
- 537 (27) Li, W.; Sidhik, S.; Traore, B.; Asadpour, R.; Hou, J.; Zhang, H.; Fehr, A.; Essman, J.; Wang, Y.;
538 Hoffman, J. M.; Spanopoulos, I.; Crochet, J. J.; Tsai, E.; Strzalka, J.; Katan, C.; Alam, M. A.;
539 Kanatzidis, M. G.; Even, J.; Blancon, J.-C.; Mohite, A. D. Light-Activated Interlayer Contraction
540 in Two-Dimensional Perovskites for High-Efficiency Solar Cells. *Nat. Nanotechnol.* **2021**.
541 <https://doi.org/10.1038/s41565-021-01010-2>.
- 542 (28) Zhang, H.; Li, W.; Essman, J.; Quarti, C.; Metcalf, I.; Chiang, W.-Y.; Sidhik, S.; Hou, J.; Fehr, A.;
543 Attar, A. Ultrafast Relaxation of Lattice Distortion in Two-Dimensional Perovskites. *Nat. Phys.*
544 **2023**, 1–6.
- 545 (29) Li, J.; Wang, H.; Li, D. Self-Trapped Excitons in Two-Dimensional Perovskites. *Front.*
546 *Optoelectron.* **2020**, *13*, 225–234.
- 547 (30) Blancon, J.-C.; Tsai, H.; Nie, W.; Stoumpos, C. C.; Pedesseau, L.; Katan, C.; Kepenekian, M.;
548 Soe, C. M. M.; Appavoo, K.; Sfeir, M. Y.; Tretiak, S.; Ajayan, P. M.; Kanatzidis, M. G.; Even, J.;
549 Crochet, J. J.; Mohite, A. D. Extremely Efficient Internal Exciton Dissociation through Edge
550 States in Layered 2D Perovskites. *Science* **2017**, *355* (6331), 1288–1292.
551 <https://doi.org/10.1126/science.aal4211>.
- 552 (31) Chen, Y.-X.; Ge, Q.-Q.; Shi, Y.; Liu, J.; Xue, D.-J.; Ma, J.-Y.; Ding, J.; Yan, H.-J.; Hu, J.-S.; Wan,
553 L.-J. General Space-Confined On-Substrate Fabrication of Thickness-Adjustable Hybrid
554 Perovskite Single-Crystalline Thin Films. *J. Am. Chem. Soc.* **2016**, *138* (50), 16196–16199.
555 <https://doi.org/10.1021/jacs.6b09388>.
- 556 (32) Leng, K.; Abdelwahab, I.; Verzhbitskiy, I.; Telychko, M.; Chu, L.; Fu, W.; Chi, X.; Guo, N.;
557 Chen, Z.; Chen, Z. Molecularly Thin Two-Dimensional Hybrid Perovskites with Tunable
558 Optoelectronic Properties Due to Reversible Surface Relaxation. *Nat. Mater.* **2018**, *17* (10), 908–
559 914.
- 560 (33) Sidhik, S.; Wang, Y.; De Siena, M.; Asadpour, R.; Torma, A. J.; Terlier, T.; Ho, K.; Li, W.;
561 Puthirath, A. B.; Shuai, X. Deterministic Fabrication of 3D/2D Perovskite Bilayer Stacks for
562 Durable and Efficient Solar Cells. *Science* **2022**, *377* (6613), 1425–1430.
- 563 (34) Stoumpos, C. C.; Soe, C. M. M.; Tsai, H.; Nie, W.; Blancon, J.-C.; Cao, D. H.; Liu, F.; Traoré, B.;
564 Katan, C.; Even, J. High Members of the 2D Ruddlesden-Popper Halide Perovskites: Synthesis,
565 Optical Properties, and Solar Cells of (CH₃(CH₂)₃NH₃)₂(CH₃NH₃)₄Pb₅I₁₆. *Chem* **2017**, *2*
566 (3), 427–440.
- 567 (35) Mao, L.; Kennard, R. M.; Traore, B.; Ke, W.; Katan, C.; Even, J.; Chabiny, M. L.; Stoumpos, C.
568 C.; Kanatzidis, M. G. Seven-Layered 2D Hybrid Lead Iodide Perovskites. *Chem* **2019**, *5* (10),
569 2593–2604. <https://doi.org/10.1016/j.chempr.2019.07.024>.
- 570 (36) Sidhik, S.; Li, W.; Samani, M. H. K.; Zhang, H.; Wang, Y.; Hoffman, J.; Fehr, A. K.; Wong, M.
571 S.; Katan, C.; Even, J.; Marciel, A. B.; Kanatzidis, M. G.; Blancon, J.; Mohite, A. D. Memory
572 Seeds Enable High Structural Phase Purity in 2D Perovskite Films for High-Efficiency Devices.
573 *Adv. Mater.* **2021**, *33* (29), 2007176. <https://doi.org/10.1002/adma.202007176>.
- 574 (37) Li, X.; Ke, W.; Traoré, B.; Guo, P.; Hadar, I.; Kepenekian, M.; Even, J.; Katan, C.; Stoumpos, C.
575 C.; Schaller, R. D.; Kanatzidis, M. G. Two-Dimensional Dion–Jacobson Hybrid Lead Iodide
576 Perovskites with Aromatic Diammonium Cations. *J. Am. Chem. Soc.* **2019**, *141* (32), 12880–
577 12890. <https://doi.org/10.1021/jacs.9b06398>.
- 578 (38) Fang, H.; Yang, J.; Tao, S.; Adjokatse, S.; Kamminga, M. E.; Ye, J.; Blake, G. R.; Even, J.; Loi,
579 M. A. Unravelling Light-Induced Degradation of Layered Perovskite Crystals and Design of
580 Efficient Encapsulation for Improved Photostability. *Adv. Funct. Mater.* **2018**, *28* (21), 1800305.
- 581 (39) Guo, Z.; Zhang, Y.; Wang, B.; Wang, L.; Zhou, N.; Qiu, Z.; Li, N.; Chen, Y.; Zhu, C.; Xie, H.;
582 Song, T.; Song, L.; Xue, H.; Tao, S.; Chen, Q.; Xing, G.; Xiao, L.; Liu, Z.; Zhou, H. Promoting
583 Energy Transfer via Manipulation of Crystallization Kinetics of Quasi-2D Perovskites for Efficient

- 584 Green Light-Emitting Diodes. *Adv. Mater.* **2021**, *33* (40), 2102246.
585 <https://doi.org/10.1002/adma.202102246>.
- 586 (40) Li, X.; Hoffman, J. M.; Kanatzidis, M. G. The 2D Halide Perovskite Rulebook: How the Spacer
587 Influences Everything from the Structure to Optoelectronic Device Efficiency. *Chem. Rev.* **2021**,
588 *121* (4), 2230–2291. <https://doi.org/10.1021/acs.chemrev.0c01006>.
- 589 (41) Katan, C.; Mercier, N.; Even, J. Quantum and Dielectric Confinement Effects in Lower-
590 Dimensional Hybrid Perovskite Semiconductors. *Chem. Rev.* **2019**, *119* (5), 3140–3192.
- 591 (42) Blancon, J.-C.; Stier, A. V.; Tsai, H.; Nie, W.; Stoumpos, C. C.; Traoré, B.; Pedesseau, L.;
592 Kepenekian, M.; Katsutani, F.; Noe, G. T.; Kono, J.; Tretiak, S.; Crooker, S. A.; Katan, C.;
593 Kanatzidis, M. G.; Crochet, J. J.; Even, J.; Mohite, A. D. Scaling Law for Excitons in 2D
594 Perovskite Quantum Wells. *Nat. Commun.* **2018**, *9* (1), 2254. [https://doi.org/10.1038/s41467-018-](https://doi.org/10.1038/s41467-018-04659-x)
595 [04659-x](https://doi.org/10.1038/s41467-018-04659-x).
- 596

597 **Acknowledgments:** The work at Rice University was supported by start-up funds under the
598 molecular nanotechnology initiative and also the DOE-EERE 2022-1652 program. J.H.
599 acknowledges the financial support from the China Scholarships Council (No. 202107990007).
600 W.L. acknowledges the National Science Foundation Graduate Research Fellowship Program
601 (This material is based upon work supported by the National Science Foundation Graduate
602 Research Fellowship Program under grant no. NSF 20-587. Any opinions, findings and
603 conclusions or recommendations expressed in this material are those of the author and do not
604 necessarily reflect the views of the National Science Foundation). Work at Northwestern on
605 perovskite solar cells is supported by the Office of Naval Research Grant N00014-20-1-2725). D.J.
606 acknowledges primary support for this work by the U.S. Army Research Office under contract
607 number W911NF-19-1-0109 and the Sloan Fellowship in Chemistry awarded by the Alfred P.
608 Sloan Foundation. S.B.A. gratefully acknowledges the funding received from the Swiss National
609 Science Foundation (SNSF) under the Early Postdoc Mobility grant (P2ELP2_187977) for this
610 work. J.E. acknowledges the financial support from the Institut Universitaire de France. The work
611 at ISCR and Institut FOTON was performed with funding from the European Union’s Horizon
612 2020 research and innovation program under grant agreement no. 861985 (PeroCUBE). This
613 research used beamline 11-BM (CMS) of the NSLS-II and the Center for Functional
614 Nanomaterials, both of which are US Department of Energy Office of Science User Facilities
615 operated for the Department of Energy Office of Science by Brookhaven National Laboratory
616 under contract no. DE-SC0012704. We thank Ruipeng Li and Esther Tsai for their assistance in
617 performing experiments at beamline CMS. J.H. acknowledges the discussion with Prof. Ming
618 Tang at Rice University and Prof. David Mitzi at Duke University.

619 **Author contributions:** J.H., J.-C.B. and A.D.M. conceived and designed the experiment. J.H. synthesized
620 the perovskite single crystals with the help of S.S.. J.H. performed 1D-XRD measurements with the help
621 of I.M., X.S. and A.M.. J.H. and H.Z. performed optical characterizations with the help of W.L. and S.B.A..
622 J.H. performed the transformation experiment. W.L. performed the machine learning analysis. J.H.
623 performed data analysis with guidance from C.K., D.J., J.-C.B., M.K., J.E., and A. D. M.. J.H. and W.L.
624 wrote the manuscript with input from everyone. All authors read the manuscript and agree to its contents,
625 and all data are reported in the main text and supplemental materials.

626 **Competing interests:** The authors declare no competing interests.